IDENTIFYING MATERIAL PARAMETERS FOR A MICRO-POLAR PLASTICITY MODEL VIA X-RAY MICRO-COMPUTED TOMOGRAPHIC (CT) IMAGES: LESSONS LEARNED FROM THE CURVE-FITTING EXERCISES

Kun Wang,[1] WaiChing Sun,[1,] Simon Salager,[2] SeonHong Na,[1] & Ghonwa Khaddour[2]*

[1]*Department of Civil Engineering and Engineering Mechanics, Columbia University, 614 SW Mudd, Mail Code: 4709, New York, New York 10027, USA*

[2]*UJF-Grenoble 1, Grenoble-INP, CNRS UMR 5521, 3SR Laboratory, 38041 Grenoble, France*

[*]Address all correspondence to: WaiChing Sun, E-mail: wsun@columbia.edu

Unlike a conventional first-order continuum model, the material parameters of which can be identified via an inverse problem conducted at material point that exhibits homogeneous deformation, a higher-order continuum model requires information from the derivative of the deformation gradient. This study concerns an integrated experimental-numerical procedure designed to identify material parameters for higher-order continuum models. Using a combination of micro-CT images and macroscopic stress–strain curves as the database, we construct a new finite element inverse problem which identifies the optimal value of material parameters that matches both the macroscopic constitutive responses and the meso-scale micropolar kinematics. Our results indicate that the optimal characteristic length predicted by the constrained optimization procedure is highly sensitive to the types and weights of constraints used to define the objective function of the inverse problems. This sensitivity may in return affect the resultant failure modes (localized vs. diffuse), and the coupled stress responses. This result signals that using the mean grain diameter alone to calibrate the characteristic length may not be sufficient to yield reliable forward predictions.

KEY WORDS: *micro-CT imaging, micro-polar plasticity, critical state, higher-order continuum, Hostun Sand*

1. INTRODUCTION

Granular matters are some of the most commonly encountered materials in our daily lives. Ranging from natural materials, such as sand, slit, gravel, fault gauges to the man-made materials, such as pills, sugar powder, and candy, granular matters may be composed of grains with various shapes, sizes, and forms. The mechanical behavior of granular assemblies are therefore not only depending on the material properties of the grains that form the assemblies, but also the evolution of the grain contact topology or fabrics (Kuhn et al., 2015; Lenoir et al., 2010; Li and Dafalias, 2011; O'Sullivan, 2011; Satake, 1993; Subhash et al., 1991; Sun et al., 2013; Walker et al., 2016; Wang and Sun, 2015). In the past decades, theoretical and numerical studies have achieved great success to describe and predict the granular materials that exhibit solid-like behavior when subjected to sufficient confining pressure. In those cases, granular materials are often treated as first-order Boltzmann continua which possess no internal microstructures or length scale. For instance, constitutive models that employ the critical state soil mechanics concept are now able to replicate the monotonic and cyclic responses of sand of different relative densities, confining pressure and initial states (Been and Jefferies, 1985; Borja and Sun, 2007; Dafalias and Manzari, 2004; Lade and Duncan, 1975; Manzari

and Dafalias, 1997; Pestana and Whittle, 1999; Schofield and Wroth, 1968; Sun, 2013; Wu et al., 1996). In these macroscopic models, microstructural attributes, such as pore size distribution, grain shapes, and size distribution, grain-scale heterogeneity are not explicitly taken into account at the grain scale. Instead, they are represented by a set of internal variables that represents the loading history. The evolution of these internal variables are then governed by phenomenological evolution laws that require material parameters calibrated from experiments. Nevertheless, the success on replicating constitutive responses at a material point level often does not automatically lead to realistic simulated responses. For instance, the classical first-order continuum model does not possess physical length scale and this may cause finite element or finite difference models to exhibit spurious mesh dependence, unless a regularization limiter is applied (Bazant et al., 1984; Belytschko et al., 1988; Fish et al., 2012; Lasry and Belytschko, 1988; Liu et al., 2015; Na and Sun, 2016; Needleman, 1988; Sun and Mota, 2014). This regularization limiter can be introduced via various means, ranging from incorporating rate dependence, inserting embedded strong discontinuity to adapting nonlocal and gradient-based constitutive relations.

For instance, classical bifurcation analysis by Rudnicki and Rice (1975) and Issen and Rudnicki (2000) can be used to predict the onset and orientation of a deformation band. Beyond the bifurcation point, additional degree of freedom that represent an embedded strong discontinuity can be introduced via assumed strain [e.g., Borja (2000)], extended finite element [e.g., Song et al. (2006)] or localization or bifurcated elements [e.g., Belytschko et al. (1988); Ortiz et al. (1987); Yang et al. (2005)]. Nevertheless, recent experimental and theoretical studies have both indicated that granular materials may initially form multiple deformation bands at the bifurcation point, but the interaction among deformation band may lead to some of the deformation band vanishing. Meanwhile, a dominated persistent shear band may emerge among them in the post-bifurcation regime (Borja et al., 2013; Gajo et al., 2004; Rechenmacher, 2006). This discovery indicates that the adaptive insertion of the enhanced mode(s) may lead to mesh bias unless there is a coarsen mechanism in place to prevent the fixture of shear band localization (Lin et al., 2015).

Opposite to the enrichment approach, higher-order continuum theory is another attractive option to circumvent the pathological mesh dependence exhibited in the Boltzmann continua. The history of generalized continuum theories can be tracked back to the work of the Cosserat brothers who published a book titled "Théorie des corps déformables in 1909" (Cosserat and Cosserat, 1909). As pointed out by Maugin and Metrikine (2010), there exist multiple interpretations and generalizations of Cosserats' work. Nevertheless, the necessary ingredients of the higher-order continuum theory are the incorporation of higher-order kinematics (micro-rotation, micro-stretch, micro-torsion, etc.) and additional internal degree of freedom that breaks the symmetry of the Cauchy stress (Eringen, 1999; Maugin and Metrikine, 2010; Mindlin, 1964). The micropolar continuum theory is a sub-class of the generalized continuum theory in which the material point is associated with micro-structures exhibiting not only deformation but changing orientations that are independent of the macroscopic deformation. These changes of orientations can be represented by Euler's angle, quaternions, and spinors, among other mathematical tools (Duhem, 1893). By incorporating the additional rotational degrees of freedom at the microscopic level, micropolar effect of granular materials, especially those associated with the onset of strain localization as observed by Desrues and Viggiani (2004); Hall et al. (2010), can be replicated properly in numerical simulations without exhibiting the spurious mesh dependence.

Nevertheless, incorporating the micropolar effect to improve the accuracy and physical underpinning of the numerical models also comes with a price. For instance, the identification of the the micropolar material parameters in addition to the non-polar counterparts can be difficult for material testing procedures that are originally designed for homogeneous specimen subjected to first-order boundary conditions. The assumption that the strain field developed inside the specimen remains approximately homogeneous in convectional triaxial and shear apparatus is unavoidably violated when high-order kinematics and couple stress are considered. These difficulties are partly responsible for the limited applications of higher-order continuum theory in engineering practices.

Our objective is to overcome this technical barrier by introducing a simple experimental-numerical method designed specifically for identifying material parameters for higher-order continua. In particular, we introduce the meso-scale kinematics data from X-ray tomographic images obtained from drained triaxial compression tests to construct a multiscale objective function. The tomographic images at selected axial strain levels are combined with the conventional macroscopic stress–strain curve and the state path to constitute the measured data set. A new objective function is then defined to simultaneously minimize the discrepancy between the simulated and measured macroscopic responses while enforcing the simulated grain-scale responses to be consistent with the kinematics information

provided by the tomographic images. Our results show that the incorporation of microstructural information from the grain scale may profoundly change the predicted length scale and failure mode of the numerical specimen. More importantly, the predicted coupled stress response is also highly sensitive to the way microstructural information is incorporated in the inverse problem.

To the best knowledge of the authors, this work is the first contribution to employ X-ray tomographic images to identify material parameters via a multiscale inverse problem for granular materials. In addition, the proposed method provides a new method to quantify the sensitivity of characteristic length predicted by material identification procedure. The findings from the Hostun sand experiment indicate that a multiscale model capable of replicating the macroscopic responses may nevertheless produce incorrect bifurcation modes and completely different micro-scale responses. This result has important implications for material modeling, as it clearly shows that calibrating macroscopic responses alone is insufficient to provide reliable forward prediction for multiscale models. In other words, a seemingly good match between experimental and simulated responses at the macroscopic level may be a consequence of high-quality grain-scale simulations or a product manufactured by excess tuning and manipulations of meso-scale material parameters.

The rest of this paper is organized as follows. In Section 2, we first describe the experimental procedure used to obtain the tomographic images. Then, the ingredients that constitute the inverse problem for a micropolar critical state plasticity model are discussed in Section 3. The calibration of a single unit cell and the finite element inverse problem are described in Sections 4 and 5, followed by a discussion of major findings. Finally, concluding remarks are given in Section 6.

As for notations and symbols, bold-faced letters denote tensors; the symbol "$\cdot$" denotes a single contraction of adjacent indices of two tensors (e.g., $\boldsymbol{a} \cdot \boldsymbol{b} = a_i b_i$ or $\boldsymbol{c} \cdot \boldsymbol{d} = c_{ij} d_{jk}$); the symbol ":" denotes a double contraction of adjacent indices of tensor of rank two or higher (e.g., $\boldsymbol{C} : \boldsymbol{\epsilon}^e = C_{ijkl} \epsilon^e_{kl}$); the symbol "$\otimes$" denotes a juxtaposition of two vectors (e.g., $\boldsymbol{a} \otimes \boldsymbol{b} = a_i b_j$) or two symmetric second order tensors [e.g., $(\boldsymbol{\alpha} \otimes \boldsymbol{\beta}) = \alpha_{ij} \beta_{kl}$]. As for sign conventions, we consider the direction of the tensile stress and dilative pressure as positive.

2. EXPERIMENTS AND MICRO-CT IMAGES FOR VALIDATIONS

This section introduces the triaxial test performed for this research at 3SR Lab and details the experimental procedures followed. The objective of performing the triaxial tests is to provide a multiscale benchmark database for model calibration and material identification. The bemchmark data consist of the macroscopic stress–strain curve and the grains position at different stress levels during the shearing, characterizing the grains-scale behavior of the granular media. These data form the basis for a multiscale objective function to search the optimal material parameters to predict the most consistent mechanical behavior measured by a weighted norm that minimizes the discrepancy between simulations and experimental observations at both grain- and specimen scales.
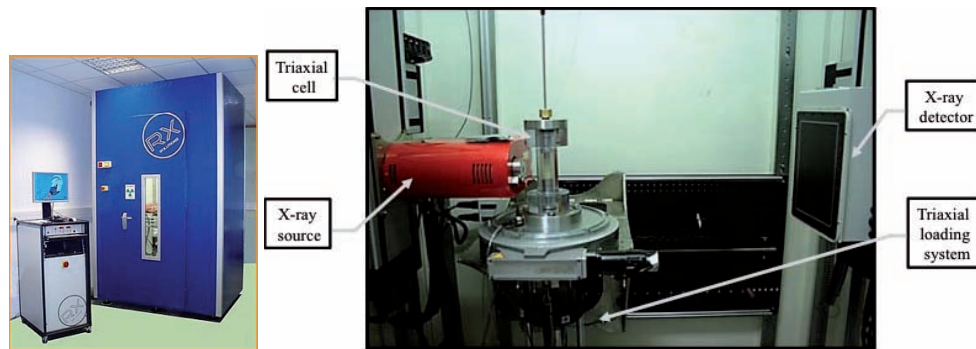
2.1 X-Ray CT

X-ray micro-CT is a non-destructive, 3D high-resolution imaging method that allows the internal structure of the scanned objects to be investigated (Andò et al., 2012; Hall et al., 2010; Lenoir et al., 2010; Sun et al., 2011). Micro-CT technology yields images that map the variation of x-ray attenuation within the objects, based on the composition of the object. Because sand and water have different x-ray attenuation coefficients, a significant contrast for the two phases is observed in an x-ray transmission image, Fig. 1. A quantitative analysis that provides detailed information on the arrangement and distribution of particles can be built from the processed 3D images.

The imaging process can be summarized as follows: the cell first is placed on a turntable stage whose rotation can be accurately controlled. An x-ray source generates a continuous x-ray beam; the beam passes through the object and casts an x-ray shadow onto the detector, see Fig. 2. The radiation that hits the detector is converted into an electronic charge, that is subsequently passed to a computer to create a radiograph (i.e., digital image). A series of images (radiographies) is acquired while rotating the object step by step through 360° at a pre-defined angular increment. These radiographies record projections that contain cumulative information on the position and density of
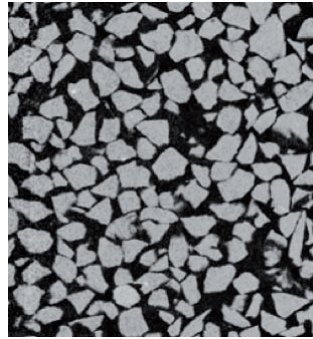
FIG. 1: Reconstructed x-ray image shows the clear contrast among grain, water, and air. The experiments in this study are performed using x-ray setup of Laboratory 3SR at Grenoble University.

FIG. 2: X-ray CT scanner at Laboratory 3SR **(left)** and the whole arrangement of triaxial setup inside x-ray cabinet **(right)**

the absorbing features within the specimen. The data obtained can be used to perform the numerical reconstruction of the final 3D image (Andò et al., 2012; Hall et al., 2010).

2.2 Triaxial Cell

The triaxial cell used in this work is designed to allow x-ray scanning and to fit to the mechanical loading system available in 3SR Laboratory. The cell is made of PMMA, which is transparent to X-rays, and quite resistant to cell pressure (confinement) applied in triaxial tests. Figure 3 shows the PMMA cell in front of X-ray source, with the specimen installed at its place inside the cell. The loading system applies and measures the axial force compressing the specimen from below, and the vertical displacement of the lower piston. The maximum axial force that can be measured by the force meter, which is in contact with the bottom of the lower piston is 0.5 kN. The measurement of the axial displacement is made by a linear variable differential transformer (LVDT) which is attached to a tie bar and measures the vertical displacement of the loading head. These measurements allow plotting the relation between the axial stress and axial shortening during the triaxial test. The speed range for the loading head is from 0.1 μm/min to 100 μm/min, which corresponds to a strain rate from 0.0005 % to 0.5% per minute (for a specimen of height 20 mm). The speed range considered in this work for the three triaxial tests is 20 μm/min (strain rate is 0.1% for a specimen of height 20 mm). The motor is driven remotely from a laptop used for data acquisition. The system of data acquisition registers the force, the confinement pressure, and LVDT measurements which were calibrated at the beginning of the test.
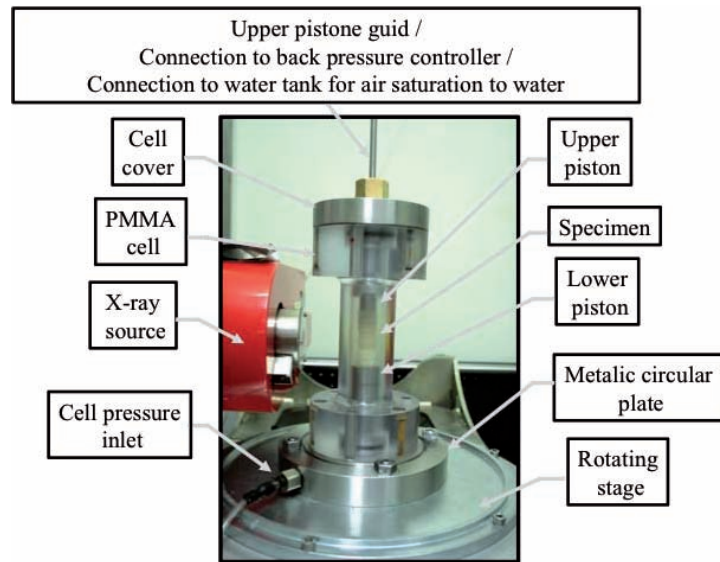
FIG. 3: PMMA cell in front of x-ray source with the specimen installed at its place inside the cell

2.3 Material Used

The experimental program is conducted on Hostun sand (HN31). Hostun sand is used as a reference material in different laboratories [cf. Amat (2008); Desrues and Andò (2015); Sadek et al. (2007)]. Its chemical components principally consist of silica ($SiO_2 > 98\%$). The grain shape is angular as shown in the scanning electron microscope image (SEM) of a few grains of Hostun sand, taken from Flavigny et al. (1990), in Fig. 4(a). A particle size distribution analysis for Hostun sand is shown in Fig. 4(b).

2.4 Specimen Preparation

The specimen prepared for the triaxial tests is a cylindrical specimen of 1 cm diameter and 2 cm height (slenderness ratio 2). The technique used for specimen preparation in the three triaxial tests is water pluviation, and thus all the
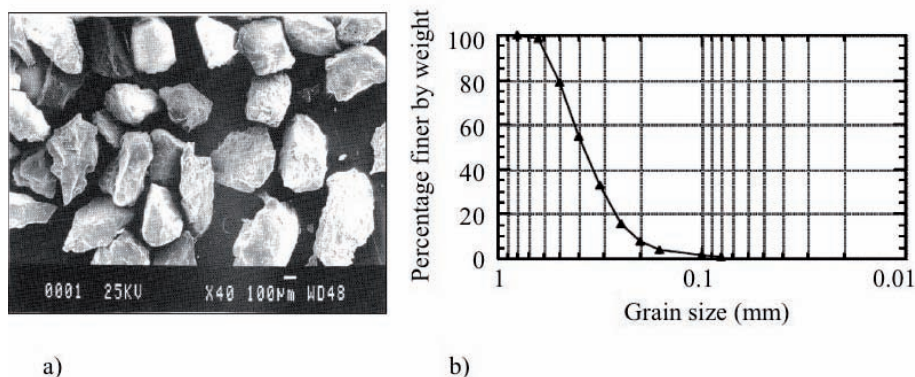

FIG. 4: (a) SEM image of Hostun sand from Flavigny et al. (Reprinted with permission from Jacques Desrues, Copyright 1990), **(b)** Grain size distribution of Hostun sand from Amat (2008)

.

pores in the specimen are completely filled with de-mineralized water in the initial state. This procedure ensures that the specimen is fully saturated at the beginning of the mechanical tests.

2.5 Macroscopic Response

The axial stress is calculated by the axial force measured over the cross section of the specimen at the initial state. The axial force comes from the raw measurement of force. The axial strain (in %) is obtained from the shortening applied by axial compression of the specimen, with respect to its initial height. The specimen behaves as expected for a dense granular material: there is a peak in the specimen's axial stress response, followed by strain softening until a plateau of residual stress is reached. The peak is reached at axial strain $\epsilon_a = 5.5\%$, and at axial stress $\sigma = 620$ kPa. The residual stress is $\sigma = 440$ kPa. Figure 5 shows the cross section of the deformed specimen at different axial strain level. While the initial deformation remains relatively homogeneous at low axial strain, the specimen subsequently deforms into a barrel shape while large strain ($\epsilon_a = 21\%$) develops toward the end of the test.

2.6 Segmentation

Measurements of the spatial distribution of grains require a separation of the solid and water phases. The volume has been "binarized" using thresholds, one between air and water peaks, and the second one between water and grain peaks. This last one is chosen in such a way that volume of voxels identified as grain phase correspond to volume of grains that has been estimated from the weight of the sample (in a dry state). The threshold between air and water is chosen to correspond to the local minimum in the gray level distribution. Figure 6 shows the cross section of the processed images of which the spatial distribution of the solid and water phases are idenified based on the threshold values.
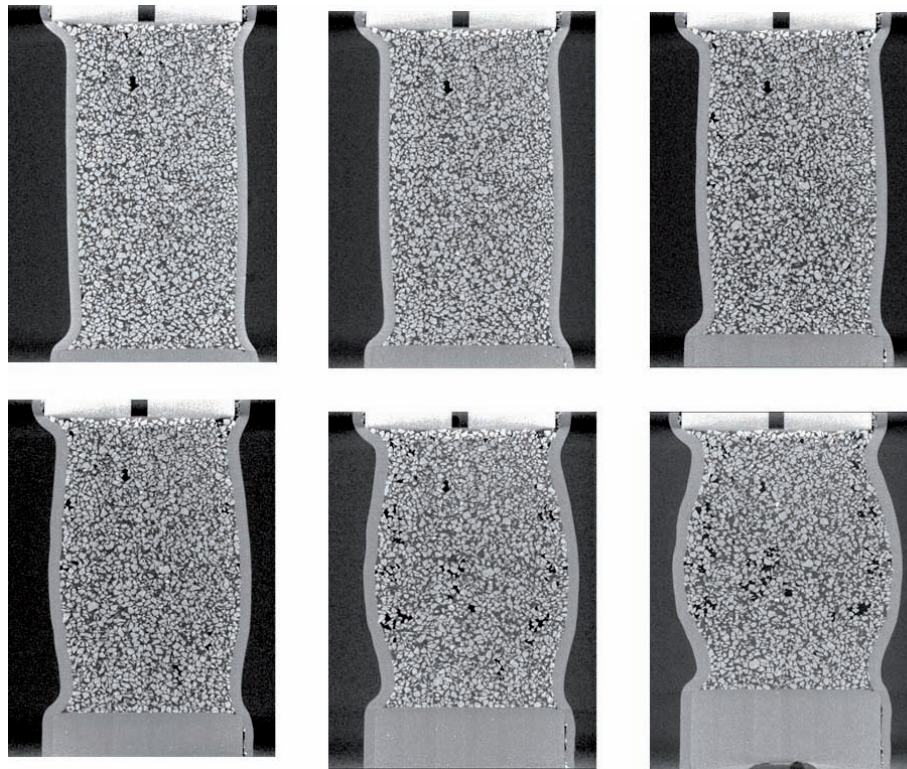
FIG. 5: Micro-CT images of the cross section of the specimen at different axial strain level
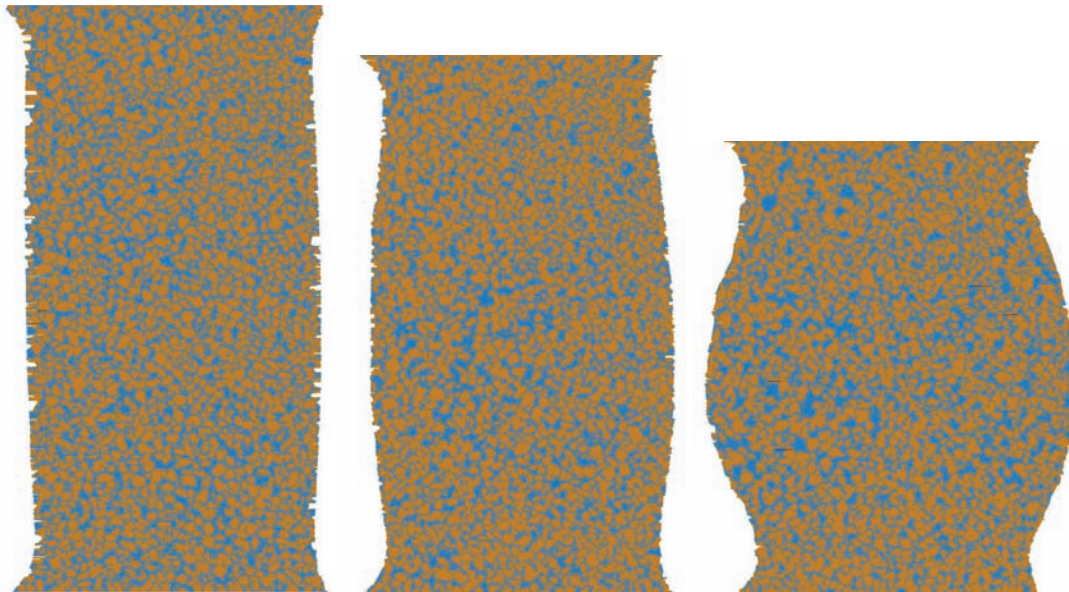
FIG. 6: Cross sections of the "binarized" two-phase images at axial strain = 0, 8, and 21%.

2.7 Grains Position

Water phase is separated from the whole 3D volume using Visilog by setting the threshold to a gray value equal to 128. In order to remove the noise inside the images, represented by water volumes of one voxel, a morphological process of erode and dilate by one voxel is applied. Later, water clusters are labeled. Labeling process can be summarized as giving each individual water cluster an Identification (Id). This Id is represented in the images by colors (i.e., each color represents a specific water cluster). The process of labeling is very useful to be able to refer to any water cluster directly by its Id number. These images where each water cluster has a specific Id and color can be considered as a mask applied to the reconstructed image (i.e., the gray-scale information is always kept). At this point, more information about water clusters is needed as the number of clusters, the center of mass, 3D volume, 3D area, ... etc. This information is obtained using another tool of Visilog "analysis individual." The measurements of clusters properties are saved in a DAT file type associated primarily with data which can be read by a text editor.

3. INVERSE PROBLEMS FOR MICROPOLAR PLASTICITY MODEL

This section presents the calibration procedure for the micropolar hypoplasticity model via the micro-CT images. The macroscopic constitutive model and the parameter identification procedure conducted via the open source toolkit Dakota [cf. Adams et al. (2009)] are briefly described. We will first treat the entire specimen as a single unit cell and we will use the gradient based approach to obtain the material parameters. The open-source optimization code Dakota is employed. Then we make use of the micro-CT images to construct the geometry of the Hostun sand sample at the beginning of the triaxial compression loading. The initial distribution of void ratio is also inferred from micro-CT information. They serve as the starting point of the model simulations. We calibrate the material parameters by two sets of benchmark data. One set consists of the macroscopic stress ratio and volumetric strain vs. the axial strain curves. The other set contains the geometry and void ratio distribution when the axial stress reaches the peak and at the residual stage.

3.1 Micropolar Finite Element Model

The inverse problem introduced in this paper is applicable to a wide spectrum of constitutive laws that considers high-order kinematics. In this study, we extend the previous two-dimensional implementation of the micropolar hypoplasticity model in Lin and Wu (2015), Lin et al. (2015) to a 3D formulation and use the 3D model to calibrate with experimental data. This model can be considered as an extension of the non-polar hypoplasticity model in Wu et al. (1996) and is suitable to characterize the Houstun sand specimen obtained for this study. For completeness, we include a brief outline of the 3D finite element formulation of the micropolar hypoplasticity model. Readers interested at the details of the micropolar hypoplasticity constitutive model may refer to Wu et al. (1996), Lin and Wu (2015), Lin et al. (2015).

The non-symmetric Cauchy stress s and the coupled stress μ are given in nonlinear path-dependent rate form in terms of the current state of the stresses, the strain rate $\dot{e}$, the curvature rate $\dot{\kappa}$, and the void ratio e. The micropolar constitutive equations writes

$$
\begin{aligned}
\overset{\circ}{s} &= C_1 tr(s)\dot{e} + C_2 tr(\dot{e})s + C_3\psi s + C_4 f_d \sqrt{||\dot{e}||^2 + l^2||\dot{\kappa}||^2}(s + s') \, , \\
\overset{\circ}{\mu} &= C_1 l^2 tr(s)\dot{\kappa} + C_2 tr(\dot{e})\mu + C_3\psi\mu + 2C_4 f_d \sqrt{||\dot{e}||^2 + l^2||\dot{\kappa}||^2}\mu \, ,
\end{aligned}
\tag{1}
$$

where $\overset{\circ}{s}$ and $\overset{\circ}{\mu}$ are the Jaumann rates of s and μ, s' is the deviatoric part of s, and

$$
\psi = \frac{tr(s \cdot \dot{e}) - tr(\mu \cdot \dot{\kappa})}{tr(s)} \, ,
\tag{2}
$$

whereas

$$
f_d = (1 - a)\frac{e - e_{\min}}{e_c - e_{\min}} + a
\tag{3}
$$

is a linear scalar function that accounts for the effect of critical state on the constitutive behavior. The material parameters to be determined are C_1, C_2, C_3, C_4, a, the critical void ratio e_c, the minimum void ratio $e_{\min}$, and the characteristic length l, which is the only additional parameter in micropolar framework compared to classical continuum hypoplasticity model. Note that this micropolar hypoplasticity model is valid under the assumption that $\dot{\kappa}$, μ, and $\overset{\circ}{\mu}$ are all skew-symmetric. An explicit numerical integration scheme (Forward-Euler) is adopted to integrate the highly nonlinear constitutive equations Eq. (1), i.e.,

$$
s_{t_1} \approx s_{t_0} + \dot{s}_{t_0}(s_{t_0}, \mu_{t_0}, \dot{e}, \dot{\kappa}, e_{t_0})\Delta t, \qquad \mu_{t_1} \approx \mu_{t_0} + \dot{\mu}_{t_0}(s_{t_0}, \mu_{t_0}, \dot{e}, \dot{\kappa}, e_{t_0})\Delta t.
\tag{4}
$$

The finite element implementation for 2D small strain problems was previously described in great detail (Lin et al., 2015). However, the 3D finite element counterpart has not yet been established. Since the tomographic images are three-dimensional and the bifurcation modes can be either symmetric or non-symmetric, an extension to three-dimensional space is necessary for comparing experimental data and simulated responses at the meso-scale level. As a result, the micropolar hypoplasticity model is implemented with a 3D micropolar finite element model. Consequently, the degrees of freedom for each node consist of three translational DOFs and three rotational DOFs, i.e., $u = [u_1 \ u_2 \ u_3 \ \phi_1 \ \phi_2 \ \phi_3]^{\mathrm{T}}$. Adopting the Voigt notation, the vectors that store the components of the generalized strain and stress tensors read

$$
\begin{aligned}
\{s\} &= [s_{11} \ s_{22} \ s_{33} \ s_{12} \ s_{21} \ s_{23} \ s_{32} \ s_{13} \ s_{31} \ \mu_{21} \ \mu_{32} \ \mu_{31}]^{\mathrm{T}} \, , \\
\{e\} &= [e_{11} \ e_{22} \ e_{33} \ e_{12} \ e_{21} \ e_{23} \ e_{32} \ e_{13} \ e_{31} \ \kappa_{21} \ \kappa_{32} \ \kappa_{31}]^{\mathrm{T}} \, .
\end{aligned}
\tag{5}
$$

The element strain-displacement matrix $\boldsymbol{B}^e$ is modified accordingly and takes the form:

$$\boldsymbol{B}^e = [\boldsymbol{B}_1, \ \boldsymbol{B}_2, \ \ldots \ \boldsymbol{B}_{n_{en}}], \qquad \boldsymbol{B}_a = \begin{bmatrix} N_{a,1} & 0 & 0 & 0 & 0 & 0 \\ 0 & N_{a,2} & 0 & 0 & 0 & 0 \\ 0 & 0 & N_{a,3} & 0 & 0 & 0 \\ N_{a,2} & 0 & 0 & 0 & 0 & N_a \\ 0 & N_{a,1} & 0 & 0 & 0 & -N_a \\ 0 & N_{a,3} & 0 & N_a & 0 & 0 \\ 0 & 0 & N_{a,2} & -N_a & 0 & 0 \\ N_{a,3} & 0 & 0 & 0 & N_a & 0 \\ 0 & 0 & N_{a,1} & 0 & -N_a & 0 \\ 0 & 0 & 0 & 0 & N_{a,1} & 0 \\ 0 & 0 & 0 & 0 & 0 & N_{a,2} \\ 0 & 0 & 0 & 0 & 0 & N_{a,1} \end{bmatrix}, \tag{6}$$

where n_{en} is the number of element nodes, N_a is the shape function of element node a, $N_{a,1}$, $N_{a,2}$, $N_{a,3}$ are the derivatives of the shape function N_a with respect to $\boldsymbol{x}_1$, $\boldsymbol{x}_2$, $\boldsymbol{x}_3$ directions in a Cartesian coordinate system. Consider a body $\mathcal{B}$ subjected to traction $\boldsymbol{t}$ and body force $\boldsymbol{b}$ partitioned into element $\mathcal{B}^e$. The matrix form of the balance of linear and angular momentum therefore reads

$$\boldsymbol{F}_{\text{INT}} = \boldsymbol{F}_{\text{EXT}}, \tag{7}$$

where

$$\boldsymbol{F}_{\text{INT}} = \mathop{\text{A}}_{e=1}^{nel} \int_{\mathcal{B}^e} \boldsymbol{B}^{e\text{T}} \cdot \boldsymbol{s} \, \text{dV} \ ; \ \boldsymbol{F}_{\text{EXT}} = \mathop{\text{A}}_{e=1}^{nel} \left(\int_{\mathcal{B}^e} \boldsymbol{N}^{e\text{T}} \cdot \boldsymbol{b} \, \text{dV} + \int_{\partial\mathcal{B}^e} \boldsymbol{N}^{e\text{T}} \cdot \boldsymbol{t} \right) \text{dV}, \tag{8}$$

where A is the assembly operator [cf. Hughes (2012)] and $\boldsymbol{N}^e = [\boldsymbol{N}_1, \boldsymbol{N}_2, \boldsymbol{N}_3, \ldots \boldsymbol{N}_{n_{en}}]$.

3.2 Optimization Algorithms for Material Parameter Identification

Material parameter identification of soil samples can be done via solving inverse problems. Previous works, such as Herle and Gudehus (1999), use multiple simple experiments, such as angle of repose, minimum and maximum index density, shear test, and oedometric compression test to identify material parameters in an almost one-by-one fashion for a non-polar hypolasticity model parameter for granular materials. Meanwhile, Ehlers and Scholz (2007) introduce a two-step staggered procedure for micropolar constitutive model for granular materials in which the identification algorithm first seeks the standard non-polar elasto-plastic material parameters from a series of cyclic triaxial tests that keeps the specimen in homogeneous states, then searches for the optimal values for the micropolar counterpart with another set of biaxial compression tests. In both approaches, the material identification procedure requires multiple mechanical tests on multiple specimens for the same materials. Nevertheless, due to the particulate nature of the granular materials, it is almost impossible to reconstruct specimens that have identical microstructural attributes.

In this work, we propose a different approach that only requires one mechanical test to identify all material parameters. Instead of using multiple tests to constitute sufficient constraints to identify all material parameters, the new approach uses tomographic imaging techniques to track the spatial variability of the void ratio and deformation and uses this kinematics information as the additional constraints for the objective function. One key assumption we made here is that the spatial relative density or porosity variation is the dominating factor for the post-bifurcation responses, but the material parameter variation is negligible. This approximated approach has been found to be successful in yielding consistent macroscopic constitutive responses and bifurcation modes for sand specimen that evolves with complex bifurcation modes. In particular, Borja et al. (2013) found that by taking account only the relative density

variation, one may correctly predict the onset of multiple shear bands at the bifurcation points, the sequential interaction mechanisms of these shear bands, and the persistent shear band that lasts till the end of the loading program.

The calibration of the micropolar hypoplasticity model is completed by finding the optimal values of the material parameters that minimize the discrepancy between the simulated results and the experimental data via iterations. How "optimal" the values of the material parameters are is determined by the specific objective function used for the inverse problem. If a global minimum of the objective function exists, then an optimization algorithm may start from differential initial guess but find the same set of optimal material parameters. In this work, we use a gradient-based method to find the optimal values of the material parameters. As a result, multiple boundary value problems are run and the results and their corresponding gradient with respect to the parametric space are computed. The objective function we used takes the following form:

$$f(\boldsymbol{x}) = \sum_{i=1}^{N} w_i \, r_i[s_i(\boldsymbol{x}), d_i]^2, \tag{9}$$

where $\boldsymbol{x}$ is the vector of all material parameters, N is the number of available experimental data for calibration, d_i is the ith data point, w_i is its weight, and $s_i(\boldsymbol{x})$ is the corresponding result obtained from model simulation using the parameter set $\boldsymbol{x}$. r_i is the residual between the simulation data $s_i(\boldsymbol{x})$ and the experimental data d_i. In this work, we normalize the residuals by defining them as the relative errors, i.e.,

$$r_i[s_i(\boldsymbol{x}), d_i] = \frac{s_i(\boldsymbol{x}) - d_i}{d_i}, \tag{10}$$

since the laboratory data we employed for parameter calibration include the stress ratio, volumetric strain, and void ratio, which are not in the same order.

In this work, we employ the Dakota analysis toolkit which provides flexible interface between simulation codes and robust optimization algorithms (Adams et al., 2009). Among the available methods we choose the gradient-based least-squares algorithm (NL2SOL) which minimizes $f(\boldsymbol{x})$ using its gradient:

$$\nabla f(\boldsymbol{x}) = \boldsymbol{J}(\boldsymbol{x})\boldsymbol{r}(\boldsymbol{x}), \qquad J_{ij} = \frac{\partial r_i}{\partial x_j} \tag{11}$$

and approximates the Hessian matrix with Gauss–Newton method:

$$\nabla^2 f(\boldsymbol{x}) = \boldsymbol{J}(\boldsymbol{x})^2. \tag{12}$$

The parameter calibration procedure requires an input file specifying the chosen optimization algorithm, the parameters to be determined, their initial values, upper and lower limits, and the experimental data set to be compared. At the beginning of each iteration, Dakota passes the current guess of the material parameters to the finite element simulation code developed for this study. The focus of this research is not the development of state-of-the-art optimization algorithm to identify material parameters. Interested readers may refer to, for instance, Mahnken and Stein (1996), Cooreman et al. (2007), Adams et al. (2009), Hu and Fish (2015) for details.

The finite element code then runs the simulations using the material parameters provided by Dakota and returns the simulation results back to Dakota to compute the discrepancy measured by the objective function, and the corresponding gradient. Based on these inputs, Dakota then determines the next iteration of material parameters and repeats the gradient estimation procedure and the discrepancy is again measured after another run of the simulation code (Adams et al., 2009). This procedure repeats until the discrepancy is below a pre-defined tolerance or when the number of iterations reaches its maximum.

4. UNIT CELL CALIBRATION

The Dakota calibration scheme is first applied to calibrate a unit cell represented by a tri-linear 8-node quadrilateral element representing the entire granular sample. This test is conducted under the additional assumptions that (1)

the specimen is composed of an effective medium of homogeneous properties inferred from the real heterogeneous specimen and (2) the deformation remains homogeneous. With these additional assumptions, the inverse problem is simplified such that only macroscopic responses from the experiment are utilized in the objective function [as demonstrated previously in Liu et al. (2016)]. The target data for curve-fitting are the stress ratio s $(\sigma_1/\sigma_3)^{\text{lab}}$ and volumetric strain e_v^{lab} along the triaxial compression test. As a result, the objective function reads

$$f(\boldsymbol{x}) = \sum_{i=1}^{N_{\sigma_1/\sigma_3}} w_i r_i \left[\left(\frac{\sigma_1}{\sigma_3} \right)_i^{\text{model}} (\boldsymbol{x}), \left(\frac{\sigma_1}{\sigma_3} \right)_i^{\text{lab}} \right]^2 + \sum_{j=1}^{N_{e_v}} w_j r_j \left[e_{v_j}^{\text{model}}(\boldsymbol{x}), e_{v_j}^{\text{lab}} \right]^2 , \qquad (13)$$

where N_{σ_1/σ_3} and N_{e_v} are the number of stress ratio data and volumetric strain data, respectively. Both data have 30 data points and the weights are equal to 1. The subscript i denotes the ith data point. The unit cell and the boundary conditions are presented in Fig. 7. The initial void ratio and the minimum void ratio are set to be 0.6, which is the average value of the sample. Note that there is no micropolar effect in this single element example, thus the material length l does not affect the macroscopic response. It is set to be equal to the element size 10 mm. The parameters to be identified via Dakota are C_1, C_2, C_3, C_4, e_c, and a.

The Dakota calibration procedure takes in total 92 evaluations, of which 72 evaluations are performed for determination of the gradient of the 6 material parameters, while the remaining 20 evaluations are making guesses based on the gradients. To demonstrate the convergence of the material parameters, the trial material parameters and the corresponding values of the objective function are presented in Table 1. The macroscopic responses obtained by the trial material parameters compared with the experimental data are shown in Fig. 8. Despite the large discrepancy between the initial guess and the laboratory results, $f(\boldsymbol{x})$ decreases rapidly: it is reduced by about 95.7% after 50 evaluations. This example demonstrates the robustness of the NL2SOL scheme in Dakota for nonlinear models and least-squares problems for which the residuals do not tend to vanish.
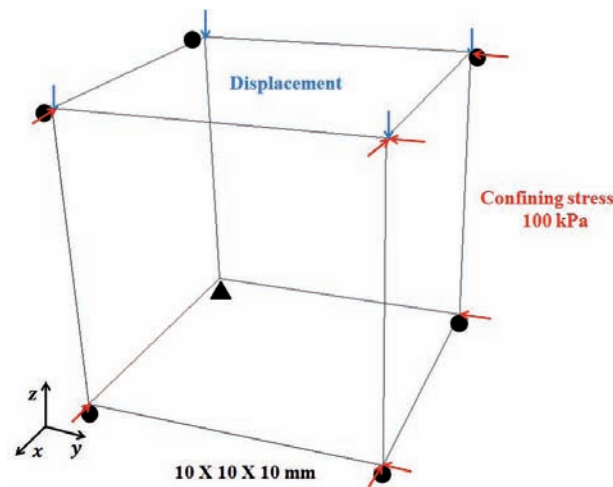

FIG. 7: Domain and boundary condition for single unit cell calibration

TABLE 1: Evolution of the material parameters during the Dakota calibration procedure

|	C_1	C_2	C_3	C_4	e_c	a	$f(\boldsymbol{x})$
Initial guess	-33.33	-104.61	-336.44	-105.90	0.800	0.900	143.77
Evaluation 20	-31.63	-62.44	-484.71	-107.15	0.650	0.905	97.60
Evaluation 50	-40.60	-1054.35	-1565.66	-138.86	0.651	0.923	6.18
Calibration result	-63.14	-1831.49	-2563.92	-237.52	0.732	0.848	2.85
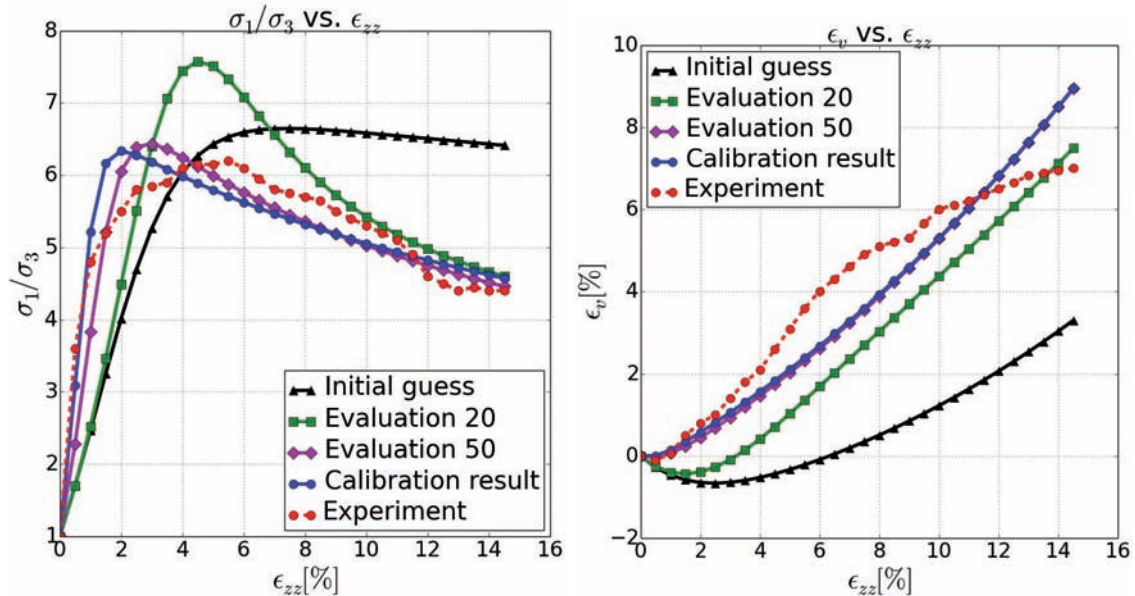
FIG. 8: Macroscopic stress ratio **(left)** and volumetric strain **(right)** responses from selected value sets of material parameters in unit cell calibration

5. MICROPOLAR HYPOPLASTIC MODEL CALIBRATION WITH MICRO-CT IMAGES FROM TRIAXIAL COMPRESSION TEST

To analyze how the spatial variability of porosity (or relative density) affects the macroscopic responses, we reconstruct a detailed 3D numerical specimen with the exact geometry and porosity distribution of the laboratory specimen using the data extracted from micro-CT image analysis. The process of converting the micro-CT experimental data into numerical specimen is illustrated in Fig. 9. After obtaining the images from the X-ray CT scan, the position and effective diameter of each grain are recorded. Three micro-CT images taken at initial (0% axial strain), peak (6% axial strain) and residual (15% axial strain) stages are used. The boundary particles are identified and thus the outer boundary of the 3D specimen can be extrapolated from the position of these particles. Following this step, the domain of the specimen is discertized by finite element and the void ratio of each finite element is calculated by established the total solid volume using the positions and effective diameters of the particles, as shown in Fig. 9.

All micro-CT based finite element simulations are performed on the numerical specimen with identified initial geometry and initial void ratio distribution. Here we adopt the hypothesis that the dominating factor that governs the transition from compressive to dilatant behavior of granular materials is the relative density or porosity, the same simplification used in Borja et al. (2013). As a result, the material parameters C_1, C_2, C_3, C_4, e_c, a, and l are assumed to be homogeneous within the specimen, while the spatial variation of the void ratio inferred from micro-CT image of the initial configuration is incorporated to study the effect of the spatial variation of void ratio. Note that the results of the inverse problem depend on how the boundary conditions are applied in model simulations. In this study, these conditions are defined based on the experimental setup with assumptions and simplifications. For example, because of the complexity of the interaction between the Hostun sand sample and the loading pistons of the triaxial cell, the top and bottom surfaces of the specimen are not fully constrained, neither in terms of the transnational nor rotational degrees of freedom (as shown in Fig. 4). In particular, we observed that the loading plates placed on the top of the specimen has slid. In this study, the authors assume that the nodal displacements on the top surface of the specimen are totally constrained, while the bottom surface is compressed under a constant strain rate in the Z direction and all nodes at the bottom boundary have the same vertical displacement in the XY plane in order that the surface area does
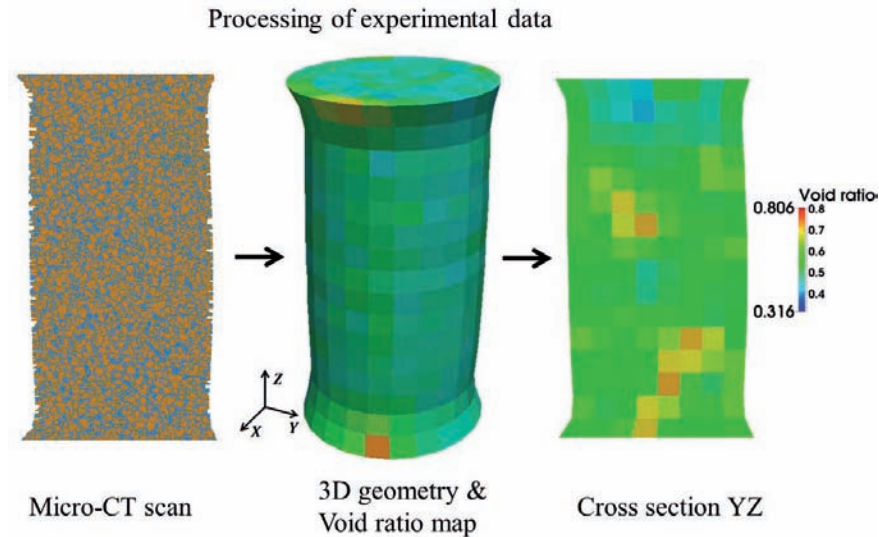
FIG. 9: Construction of the numerical sample and void ratio distribution from micro-CT experimental data at the initial stage (0% axial strain) of the triaxial compression test

not change. This constraint is applied via the Lagrange multipliers. Meanwhile, the rotations on both surfaces are prohibited. The lateral surface of the FEM model is under constant confining pressure of 100 kPa and is free to rotate, neglecting the effect of the rubber membrane in the testing apparatus.

The Dakota calibration procedure of the material parameters is carried out for two inverse problems. In the first problem (Case A), only the macroscopic responses serve as the constraints for material parameters. The second problem (Case B) takes into account, in additional to the macroscopic constitutive responses, the local void ratio developed at the peak and residual stages, thus adopting information from micro-CT images as additional target. The weight of the void ratio data in Case B is intentionally set larger than the macroscopic data such that the microstructural evolution can be compatible. These two extreme cases are studied to separate the influence of either macroscopic behavior or meso-scale behavior on the parameter calibration. In the third numerical experiments, we introduce a new multiscale objective function that takes account of both macroscopic and meso-data in a more balanced way. We then reuse the calibrated material parameter sets from Case A and Case B as the initial guesses for the restarted material parameter identification procedure to study the sensitivity of the calibration procedure.

5.1 Case A: Results from Macroscopic Objective Function

The objective function for Case A is the same as Eq. (13), which only consists of macroscopic stress ratio and volumetric strain data. Both data types contain 30 data points, thus their weights are identical. Unlike elasto-plastic models for granular materials, the micropolar hypoplastic constitive model does not separate elastic and plastic parameters. Thus the material parameters are calibrated simultaneously, not in a stepwise manner (Ehlers and Scholz, 2007). The initial guess of the material parameters and the calibrated results in Case A is presented in the Table 2. The macroscopic responses obtained by the parameter sets from initial guess, the 20th evaluation, the 50th evaluation, and the final calibration result are compared in Fig. 10. The evolution of the curves shows that the iterations converge to the final solution that minimizes the objective function. However, the local void ratio distribution does not converge to the actual experiment data. This is shown in Fig. 11 where the experimental data of void ratio map in cross-section YZ and the relative error map [defined in Eq. (10)] computed from simulations are presented. Since the sample geometry and void ratio distribution are not included in the objective function of Case A, the calibration procedure does not correct the void ratio discrepancy with the initial guess and leads to a numerical solution that a dominant shear band

TABLE 2: Calibration of material parameters of entire sample using Case A: only macroscopic responses; Case A1: equal weights of stress ratio, volumetric strain and local void ratio data, starts from results of Case A; Case B: macroscopic responses and local void ratio distributions; Case B1: equal weights of stress ratio, volumetric strain and local void ratio data, starts from results of Case B

|	Number of iterations	C_1	C_2	C_3	C_4	e_c	a	l
Initial guess	—	-68.00	-767.60	-2742.70	-257.50	0.650	0.980	0.200 mm
Case A	74	-70.57	-832.40	-2524.10	-261.70	0.637	0.960	0.468 mm
Case A1	30	-69.67	-1372.67	-2075.62	-251.90	0.641	0.976	0.364 mm
Case B	117	-67.21	-920.08	-2312.79	-259.45	0.636	0.971	0.977 mm
Case B1	30	-67.91	-1229.29	-2244.82	-262.41	0.6358	0.970	0.979 mm
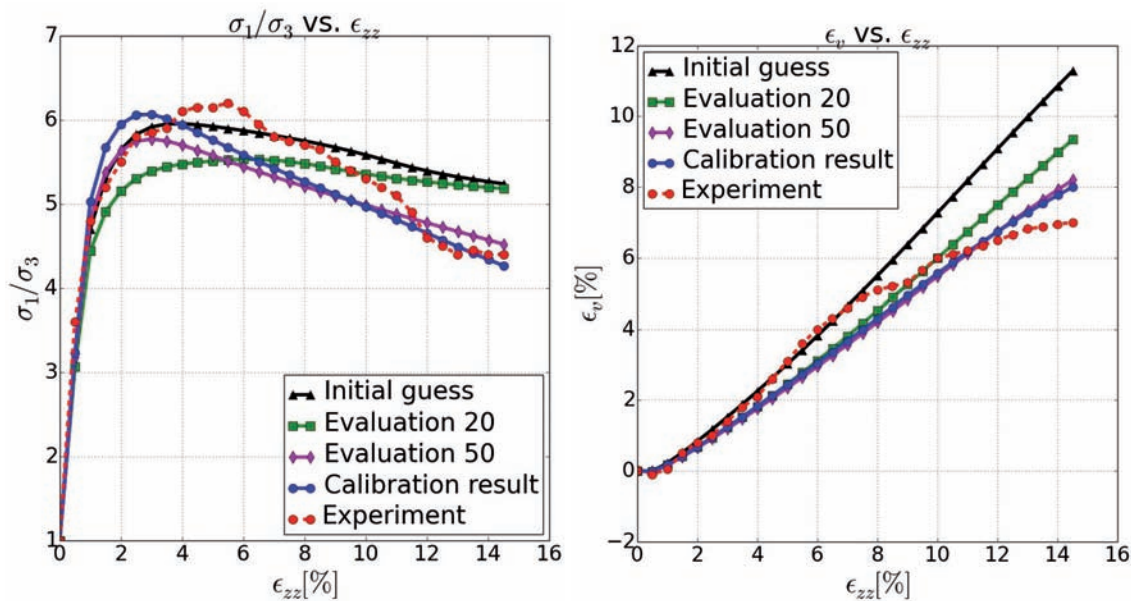
FIG. 10: Stress ratio and volumetric strain responses of full sample simulation during the calibration procedure using only macroscopic responses (Case A)

is formed inside the sample, while the actual specimen developed a "barrel" shape that exhibit diffusive bands (Ikeda et al., 2003).

In the correction step (Case A1), we modify the objective function used as previous calibrated material parameters set as an initial guess. This modified objective function incorporates additional terms to constrain the material parameter set such that the numerical specimen also exhibits the same peak and residual shear strength due to the last two terms in (14), which reads

$$
\begin{aligned}
f_2(\boldsymbol{x}) = {} & \frac{1}{N_{\sigma_1/\sigma_3}} \sum_{i=1}^{N_{\sigma_1/\sigma_3}} w_i r_i \left[\left(\frac{\sigma_1}{\sigma_3}\right)_i (\boldsymbol{x}), \left(\frac{\sigma_1}{\sigma_3}\right)_i^{\text{lab}} \right]^2 + \frac{1}{N_{e_v}} \sum_{j=1}^{N_{e_v}} w_j r_j \left[e_{v_j}(\boldsymbol{x}), e_{v_j}^{\text{lab}} \right]^2 \\
& + \frac{1}{N_{\text{element}}} \sum_{k=1}^{N_{\text{element}}} w_k r_k \left[e_k^{\text{peak}}(\boldsymbol{x}), e_k^{\text{peak}^{\text{lab}}} \right]^2 + \frac{1}{N_{\text{element}}} \sum_{m=1}^{N_{\text{element}}} w_m r_m \left[e_m^{\text{residual}}(\boldsymbol{x}), e_m^{\text{residual}^{\text{lab}}} \right]^2 ,
\end{aligned}
\tag{14}
$$
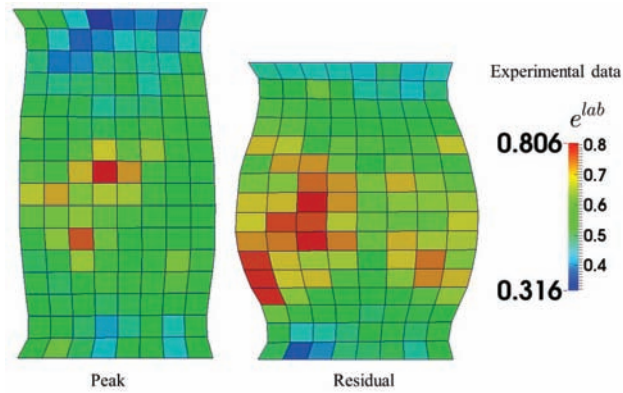
(a) Void ratio distribution from Micro-CT images
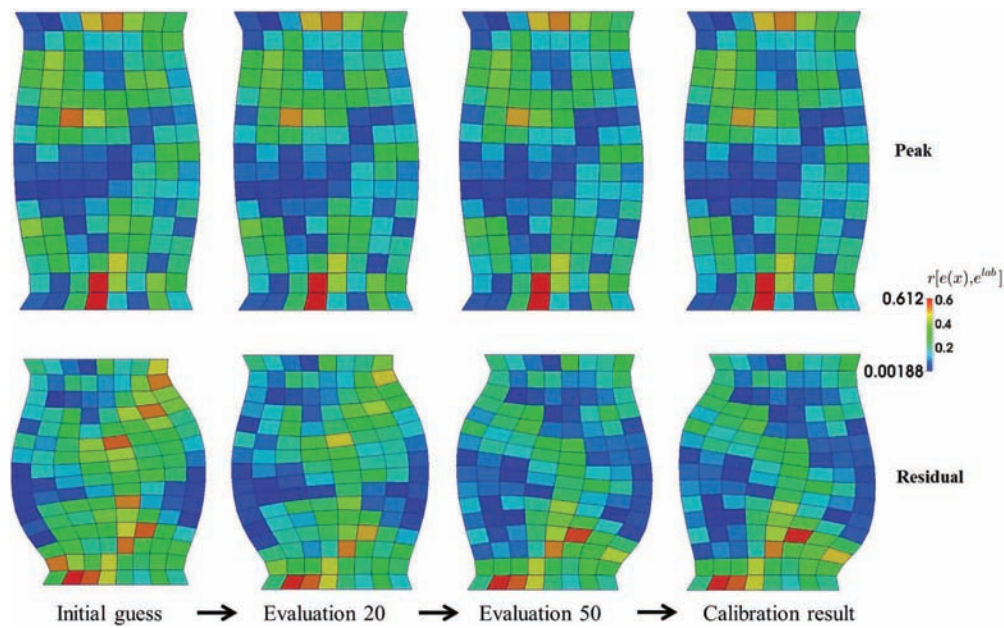
(b) Distribution of residuals [defined in Eq. (10)] at selected steps of the Dakota calibration in Case A

FIG. 11: Relative error of local void ratio distribution between full sample simulation and micro-CT data (shown in cross section in plane YZ) during Dakota calibration procedure using Case A: only macroscopic responses

where e_i are void ratio in element i, N_{element} is the number of elements in the FEM model. The contributions of stress ratio, volumetric strain, local void ratio data are balanced by the number of data points of each type. The weights of each data type equal to 1.

5.2 Case B: Results from Multiscale Objective Function

The objective function for Case B takes the form

$$f_2(\boldsymbol{x}) = \sum_{i=1}^{N_{\sigma_1/\sigma_3}} r_i \left[\left(\frac{\sigma_1}{\sigma_3}\right)_i (\boldsymbol{x}), \left(\frac{\sigma_1}{\sigma_3}\right)_i^{\mathrm{lab}} \right]^2 + \sum_{i=1}^{N_{e_v}} r_i \left[e_{v_i}(\boldsymbol{x}), e_{v_i}^{\mathrm{lab}} \right]^2$$

$$+ \sum_{i=1}^{N_{\mathrm{element}}} r_i \left[e_i^{\mathrm{peak}}(\boldsymbol{x}), e_i^{\mathrm{peak^{lab}}} \right]^2 + \sum_{i=1}^{N_{\mathrm{element}}} r_i \left[e_i^{\mathrm{residual}}(\boldsymbol{x}), e_i^{\mathrm{residual^{lab}}} \right]^2 . \tag{15}$$

In this function, the residuals of all available experimental data point are treated equally in the objective function. Since the number of elements is much larger than the number of stress ratio and volumetric strain data, the objective function Eq. (15) has much larger weight on micro-CT data than the macroscopic responses. The calibration procedure in Case B employs the same initial guess of the material parameters previously used in Case A. The calibrated results are also shown in Table 2 to show comparisons. Compared to other hypoplastic material parameters, the material length parameter l, which accounts for the micropolar effect in the model, varies more significantly when experimental data of local void ratio are included in the least square problem. The macroscopic responses obtained by the parameters sets from initial guess, the 20th evaluation, the 50th evaluation, and the final calibration result are compared in Fig. 12. Although the volumetric strain response approaches the experiment data along the iterations, the macroscopic stress ratio response deviates from the experimental response in the sense that the peak stress and residual stress do not coincide and the softening phenomenon is not apparent. As for the meso-scale data shown in Fig. 13, the calibrated parameters lead to a deformed configuration much closer predication to actual specimen geometry than that of the Case A results shown in Fig. 11. In particular, the Case B calibrated simulation correctly predicts the increased of porosity at the middle of specimen, which is consistent to the observation in the laboratory. The Case A calibrated simulation leads to porosity increase highly concentrated in a single persistent anti-symmetric shear band that was not triggered in the actual experiment. This observation indicates the necessity of including micro-structural information in material parameter identification procedures. Note that the relative errors of void ratio near the top and bottom surfaces, unlike the central areas, are not significantly reduced during the Dakota calibrations. This is because the boundary conditions in model simulation does not perfectly represent the experimental setup.

The objective function Eq. (14) is again adopted to perform the correcrtion step from the calibrated results (Case B1). The correction is made by using the equilibrium weights of different types of experimental data. The
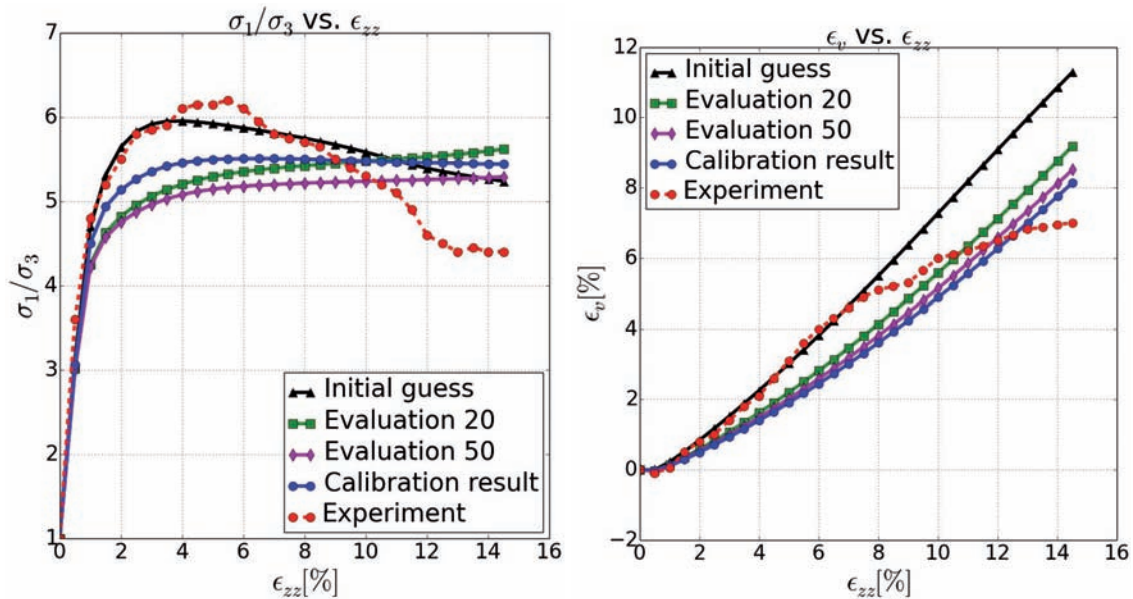
FIG. 12: Stress ratio and volumetric strain responses of full sample simulation during the calibration procedure using macroscopic responses and local void ratio distribution (Case B)

Distribution of residuals at selected steps of the Dakota calibration in Case B
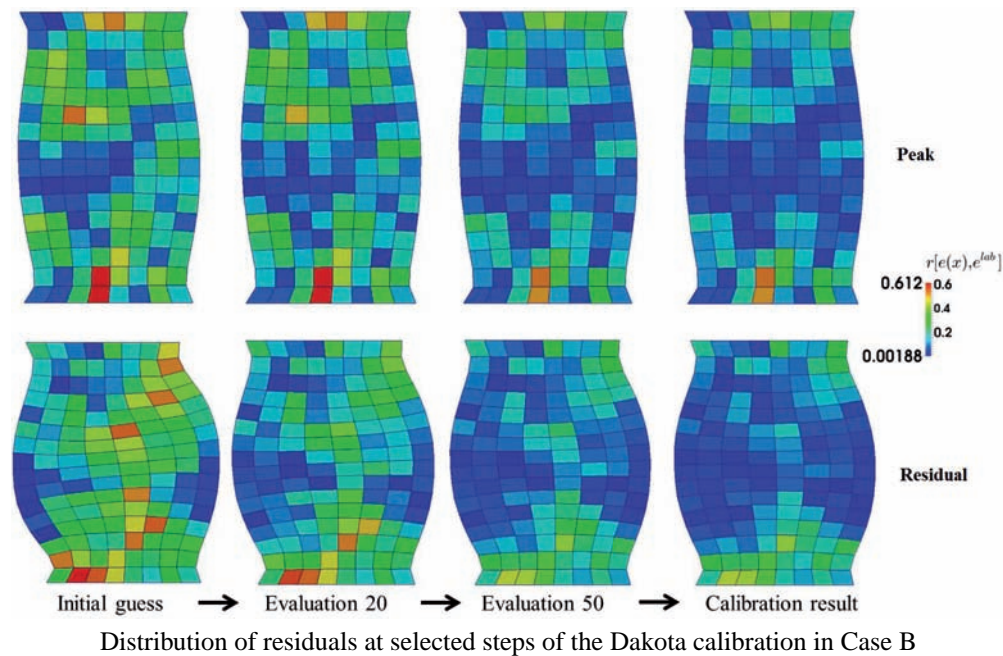
FIG. 13: Relative error of local void ratio distribution between full sample simulation and micro-CT data (shown in cross section in plane YZ) during Dakota calibration procedure using Case B: macroscopic responses and local void ratio distribution

results are recapitulated in Table 2 and the macroscopic responses in different cases are compared in Fig. 14. Recall that in the correction step Case A1, the prediction of peak stress has been improved. In this case, the discrepancy between the model response and experimental data in Case B1 has not been improved or even changed significantly in the correction step, which indicates that both objective functions Eqs. (15) and (14) have similar local minimizers.

5.3 Discussion

Two calibration strategies are employed in this study. The resultant material parameters and calibrated simulations are analyzed. In the first strategy, we find material parameter that allows the finite element simulations to replicate the macroscopic responses as close as possible, but neglect all meso-scale information provided by the micro-CT images. This optimized material parameter set (optimized in terms of macroscopic responses only), are then used as the initial guess of the next inverse problem. Following this predictor step, another inverse problem is defined by a new multiscale objective function that takes account of both the macroscopic data and local void ratio properties used for calibration. This approach mimics the idea in Ehlers and Scholz (2007) for determining material parameters for micropolar constitutive laws. The major departure here is the usage of micro-CT image and the elimination of the need to use multiple experimental tests to generate constraints for the objective function. To analyze the importance of the initial guess and whether a global optimal value for the material parameter set exists, we employ another alternative strategy in which the meso-scale information is used right at the predictor step. Then, the same multiscale objective function used in the corrector step [i.e., Eq. (14)] is used to balance the weights of global and local data.

5.3.1 Comparisons of Results

At the first look, the approach that starts with calibrating macroscopic parameter seems to be better in terms of replicating compatible shear stress history as shown in Fig. 14(a), even though both calibrated finite element simulations yield
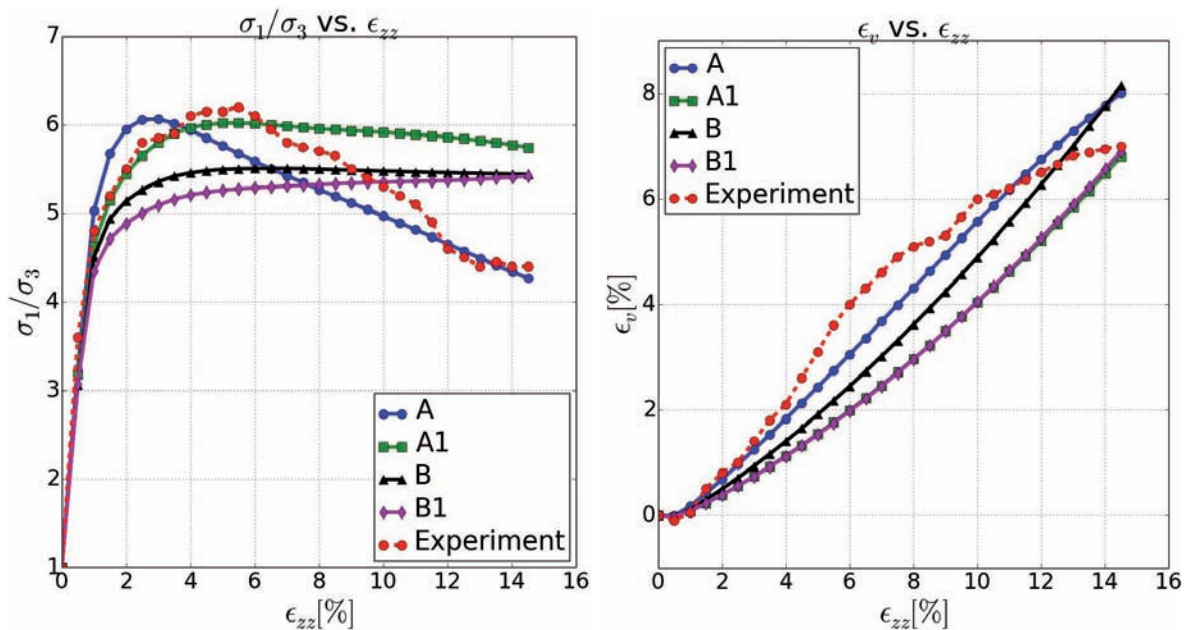
FIG. 14: Stress ratio and volumetric strain responses of full sample simulation during the calibration procedure using Case A: only macroscopic responses; Case A1: equal weights of stress ratio, volumetric strain, and local void ratio data, starts from results of Case A; Case B: macroscopic responses and local void ratio distribution; Case B1: equal weights of stress ratio, volumetric strain, and local void ratio data, starts from results of Case B

similar volumetric responses. In particular, the second approach is unable to capture the macroscopic peak and residual shear stresses at the predictor step, and again fails to make any significant improvement in capturing the peak and residual shear strength after switching to the multiscale objective function, as shown in Fig. 14. As a result, evidence provided in the macroscopic responses seems to favor the staggered approach similar to the one proposed in Ehlers and Scholz (2007) in which the calibration process begins with an inverse problem that first curve-fit macroscopic behaviors, followed by a correction step that uses multiscale objective function to enforce consistency of kinematics.

However, a closer look at the deformed configuration and the meso-scale responses may lead to an opposite conclusion. In particular, we find that the weight modification approach that begins with calibrating meso-scale information from micro-CT images actually yields the experimentally observed bifurcation mode, while the macro-then-microscopic approach does not. In Case A, $l = 0.468$ mm, which is close to the mean particle diameter $d_{50} = 0.338$ mm, a persistent shear band has developed in the specimen. This persistent shear band is non-symmetric and has not been observed in the micro-CT images captured during the drained triaxial compression test. In Case B, however, $l = 0.977$ mm, which is 2.5 times larger than the mean particle diameter and the barrel-shaped deformed specimen develops a barrel deformed configuration followed by the development of an X-shaped shear localization zone. These kinematic features are consistent with what is observed in the physical experiment, even though the Case B simulation does not replicate the shear stress responses as close as the Case A simulation does.

In other words, the set of material parameters that leads to the best replica of macroscopic responses observed in laboratory does not necessarily yield the correct bifurcation mode. As a result, the reasonable strategy is to design an objective function that acts as a compromise between matching macroscopic responses and maintaining consistent kinematics at meso-scale level. Furthermore, the notable difference in the macroscopic and microscopic responses predicted by the staggered approach and weight modification approach indicates that the calibration exercise is highly path-dependent and multiple local minima are likely to exist, thus making it difficult to find the global minimum point for the multiscale objective function in the parametric space.

5.3.2 Source of Error

The discrepancy between the experimental data and simulation results may also be attributed to the idealized boundary condition applied on numerical specimen. In particular, the specimen-loading-plate interaction between the sample and the loading pistons as well as the elastic membrane are not accurately and explicitly modeled (Albert and Rudnicki, 2001). Moreover, the assumption that material parameters are homogeneous throughout the specimen may also oversimplify the spatial variability of the physical specimens. Finally, the micropolar finite element model is formulated using the Jaumann rate of the Cauchy stress. The Jaumann rate is an objective rate which is suitable for materials in the geometrical nonlinear regime with small strain and large rotation. However, some previous works, such as Molenkamp (1986), have pointed out that the Jaumann rate should be avoided for problems with large deviatoric strain. These limitations will be considered in future studies.

### 5.3.3 Length Scale, Higher-Order Kinematics and Bifurcation Modes

The higher-order quantities, namely the curvature κ and the coupled stress μ, can be computed from the micropolar model simulation, while this information is not available from micro-CT images. In this study, two types of shear bands are encountered with different material parameters in the finite element simulations even though both simulations began with the same initial geometry and void ratio distribution. In Case A and B, the calibrated material length l varies significantly, compared to other material parameters.

In both cases, the distribution of the norm of the couple stress tensor $|\mu| = \sqrt{\mu_{21}^2 + \mu_{32}^2 + \mu_{31}^2}$ and the norm of the curvature tensor $|\kappa| = \sqrt{\kappa_{21}^2 + \kappa_{32}^2 + \kappa_{31}^2}$ are shown in Figs. 15 and 16, respectively. The coupled stress and curvature localize in the transition zone between the shear localization region and homogeneously deformed region, suggesting that the micropolar effect becomes very important when high-gradient deformation occurs in granular materials. This observation is consistent with numerical experiments conducted with discrete element method (Ehlers et al., 2003; Oda and Iwashita, 2000; Wang and Sun, 2016a,b).

The evolution of shear bands simulated in Case A and Case B is illustrated in Fig. 17 using color map of $|\mu|$, as well as in Fig. 18 using color map of $|\kappa|$. At the beginning of the triaxial loading, two-axes symmetric localization patterns emerge for both simulations (Ikeda et al., 2003). After the peak stress of Case A (at 3% axial strain), the pattern bifurcates to an asymmetry pattern: one shear band becomes stronger than the other. Upon further loading, the dominant shear band becomes persistent and the other weak band gradually dies out. As for Case B, the two bands compete with each other along the deformation but neither predominates. The initial pattern bifurcates to bilateral symmetry so that the symmetry with respect to the horizontal axis is broken. The diffuse mode is preserved to the end

(a) Case A   (b) Case B
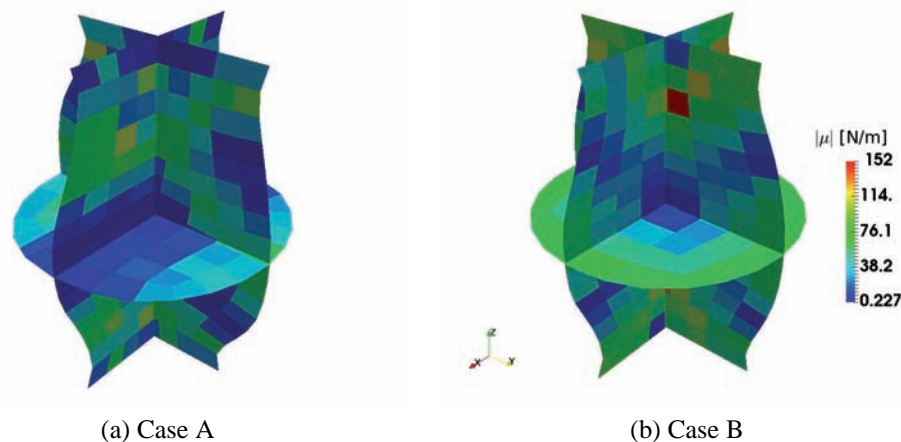
FIG. 15: Norm of the coupled stress tensor $|\mu| = \sqrt{\mu_{21}^2 + \mu_{32}^2 + \mu_{31}^2}$ for results of inverse problems A and B at the residual stage

(a) Case A   (b) Case B
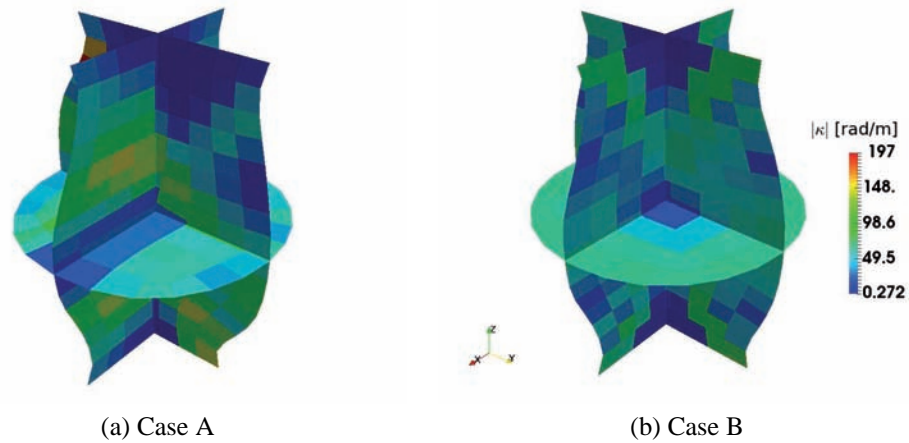
FIG. 16: Norm of the curvature tensor $|\kappa| = \sqrt{\kappa_{21}^2 + \kappa_{32}^2 + \kappa_{31}^2}$ for results of inverse problems A and B at residual stage
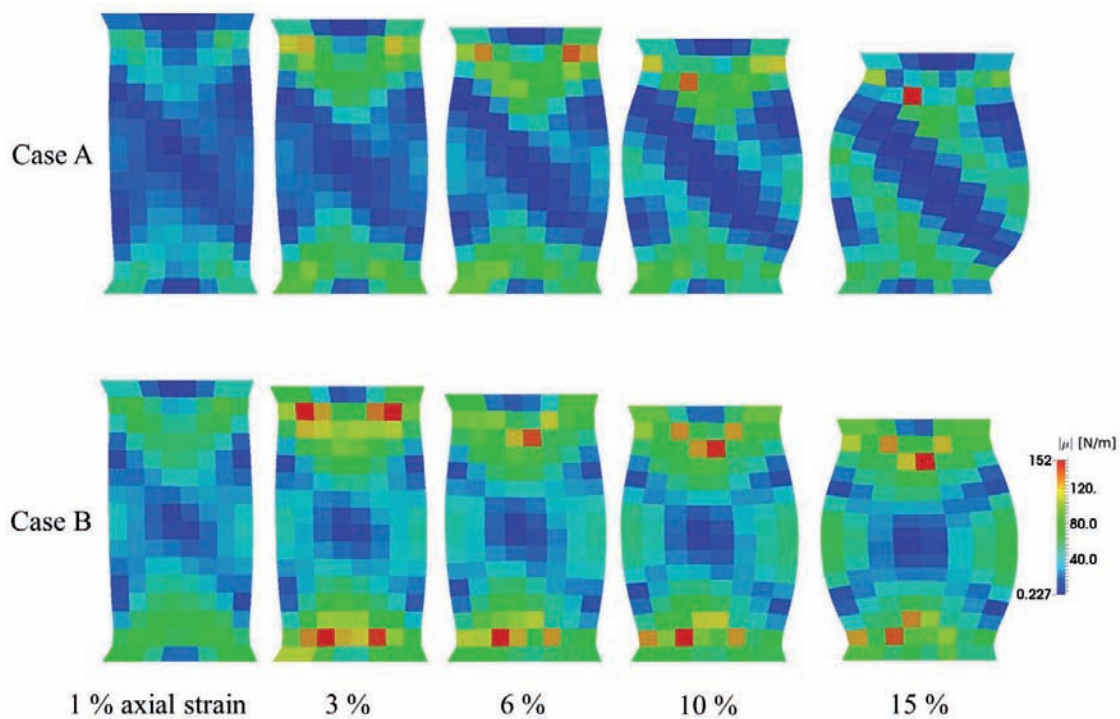
FIG. 17: Evolution of shear localization in cross section YZ of calibraion results of Case A and Case B, illustrated in the norm of coupled stress

of the loading. This analysis shows that, even though the spatial variability of the material parameters is neglected, the numerical values of the material parameters, particularly the material length l, still impose strong effects on the failure mode of numerical specimen.
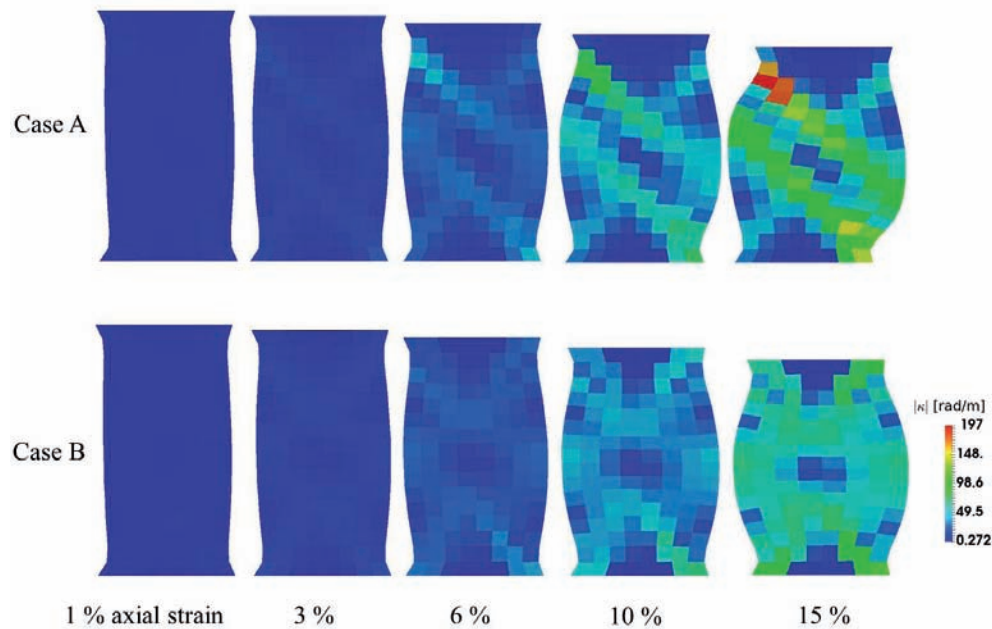
FIG. 18: Evolution of shear localization in cross section YZ of calibraion results of Case A and Case B, illustrated in the norm of curvature tensor

5.3.4 Critical State

The anisotropy density function f_d of Eq. (3) is an indicator of the critical state, a condition at which particulate materials keep deforming in shear at constant void ratio and stress (Casagrande, 1936; Roscoe et al., 1958). In the micropolar hypoplasticity adopted in this study, the local void ratio approaches the critical void ratio e_c, f_d approaches 1. The distribution of f_d of the two numerical specimens captured at residual stage of Cases A and B are presented in Fig. 19. Since the different calibrated material parameters are used in Case A and B, the failure modes as well as the locations where the Hostun sand first reaches the critical state are also different. In Case A, the elements residing in the persistent shear band are close to the critical state, while the elements outside the zone are not close to it. In Case B, the pattern of f_d also coincides with the diffuse failure mode presented in Fig. 17, showing that the unit cells inside the shear band are also closer to critical state than the host matrix, but the difference between the numerical value of f_d within the host matrix and inside the shear band are less significant than Case A. Both findings are consistent with Tejchman and Niemunis (2006); Wang and Sun (2016b) where the strain localization triggered by the material bifurcation in dense assemblies tends to have the void ratio approaching its critical value locally, but the specimen itself does not necessarily reach critical state globally. Comparing this observation with the coupled stress norm shown in Fig. 17, we observed that the shear band is not only much closer to the critical state, but also has significantly lower coupled stress magnitude. This result is consistency with the norm of the curvature tensor shown in Fig. 18 where the specimen has significant amount of micro-rotation at the boundary of the shear band and the host matrix but the micro-polar kinematics is not significant inside the shear band and in the host matrix.

6. CONCLUSIONS

In this work, we incorporate information obtained from both macroscopic measurement and meso-scale kinematics to analyze the sensitivity of the predicted characteristic length and mechanical responses of a 3D micropolar hypoplasticity finite element model. To the best knowledge of the authors, this is the first contribution that incorporates micro-CT
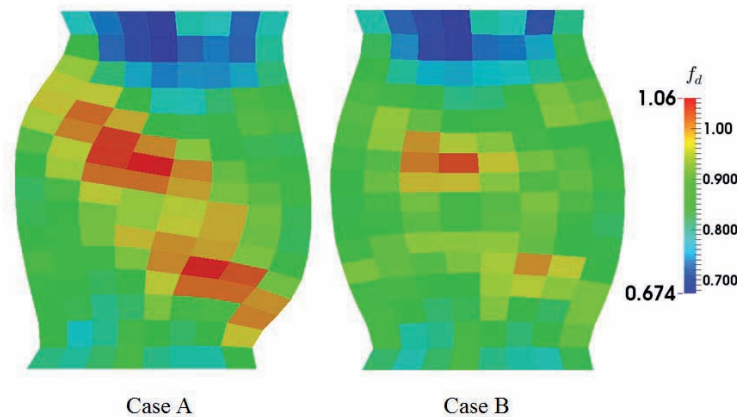
FIG. 19: Distribution of f_d for results of inverse problems A and B at the residual stage. $f_d = 1$ indicates that the material is in critical state.

images and multiscale objective function into the material parameter identification procedure for micropolar plasticity for granular materials.

The results show that the incorporation of meso-scale information may significantly change the predicted length scale obtained from the inverse problems and leads to different bifurcation modes in the finite element simulations. Even though similar macroscopic responses are observed from simulations conducted with single-scale and multiscale objective functions, the macroscopic responses in the former case may yield meso-scale responses that are not consistent with those of the real specimen. As a result, the apparently good curve-fitting of macroscopic response is not a good indicator of forward prediction capacity. This result has important implications for the validations of grain-scale simulation tools (such as discrete element, lattice-beam, and lattice spring models) in which macroscopic stress–strain responses are often the only experimental data available for benchmark and validations. The numerical results, particularly the difference of the failure modes obtained from different objective functions, indicate that using macroscopic stress–strain curve alone to evaluate or validate grain-scale simulations is neither productive nor reliable.

Although the higher-order quantities, the curvature κ and the coupled stress μ, are not available from micro-CT images, they are computed from the micropolar simulations with the material parameters optimized for different objective functions. Depending on which set of material parameters is employed, the numerical specimen may either develop a persistent shear band, which is not observed in the experiment, or a diffuse failure mode, which is observed from micro-CT images. Comparisons between the simulation results with micro-CT images suggest that a staggered predictor–corrector procedure that first employs the macroscopic objective function to curve-fit the macroscopic responses, then use the multiscale objective function to enforce kinematic constraints seem to yield a more compatible macroscopic constitutive response with the experimental counterpart, but the material parameters that lead to the best curve-fitting macroscopic responses also lead to an incorrect bifurcation mode. This finding is alerting, as the material parameters that lead to the wrong bifurcation mode in the backward calibration exercise is also likely to generate even more unrealistic forward prediction. The apparently good match in the macroscopic curve can be misleading and generate a false sense of confidence for the numerical model. This is a noteworthy concern, as there is an alerting trend in which the forward-predictive capacity of grain-scale models are often incorrectly measured by how well they curve-fit the macroscopic stress–strain curve, rather than how well they are able to generate compatible and consistent mechanical behaviors across length scales. The issue associated with this calibration approach is not apparent when calibration is conducted at the unit cell level in which only homogeneous deformation is considered. However, when macroscopic stress–strain curve is used to calibrate meso-scale or grain-scale models, the dimensions of the parametric space can be larger than the number of constraints provided by the macroscopic responses. The insufficiency of constraints then makes it possible to generate simulations that apparently match the macroscopic calibration with a

completely inconsistent microstructure. By incorporating microscopic information from micro-CT images to calibrate material parameters, this research provides important evidence to suggest that constraining micro-mechanical model to match macroscopic responses is not sufficient. Nor is it a meaningful way to measure the quality of numerical predictions. These lessons are important for the calibration and validation of high-order and multiscale finite element models.

ACKNOWLEDGMENTS

REFERENCES

Adams, B. M., Bohnhoff, W. J., Dalbey, K. R., Eddy, J. P., Eldred, M. S., Gay, D. M., Haskell, K., Hough, P. D., and Swiler, L. P., Dakota, a multilevel parallel object-oriented framework for design optimization, parameter estimation, uncertainty quantification, and sensitivity analysis: Version 5.0 users manual, *Sandia National Laboratories, Tech. Rep. SAND2010-2183*, 2009.

Albert, R. A. and Rudnicki, J. W., Finite element simulations of tennessee marble under plane strain laboratory testing: Effects of sample–platen friction on shear band onset, *Mech. Mater.*, vol. **33**, no. 1, pp. 47–60, 2001.

Amat, A. S., *Elastic Stiffness Moduli of Hostun Sand*, PhD thesis, Universitat Politècnica de Catalunya, Escola, Tècnica Superior d'Enginyers de Camins, Canals i Ports de Barcelona, Departament d'Enginyeria del Terreny, Cartogràfica i Geofísica, (Enginyeria Geològica), 2008.

Andò, E., Hall, S. A., Viggiani, G., Desrues, J., and Bésuelle, P., Grain-scale experimental investigation of localised deformation in, sand: a discrete particle tracking approach, *Acta Geotech.*, vol. **7**, no. 1, pp. 1–13, 2012.

Bazant, Z. P., Belytschko, T. B., and Chang, T.-P., Continuum theory for strain-softening, *J. Eng. Mech.*, vol. **110**, no. 12, pp. 1666–1692, 1984.

Been, K. and Jefferies, M. G., A state parameter for sands, *Géotechnique*, vol. **35**, no. 2, pp. 99–112, 1985.

Belytschko, T., Fish, J., and Engelmann, B. E., A finite element with embedded localization zones, *Comput. Methods Appl. Mech. Eng.*, vol. **70**, no. 1, pp. 59–89, 1988.

Borja, R. I., A finite element model for strain localization analysis of strongly discontinuous fields based on standard galerkin approximation, *Comput. Methods Appl. Mech. Eng.*, vol. **190**, no. 11, pp. 1529–1549, 2000.

Borja, R. I. and Sun, W. C., Estimating inelastic sediment deformation from local site response simulations, *Acta Geotech.*, vol. **2**, no. 3, pp. 183–195, 2007.

Borja, R. I., Song, X., Rechenmacher, A. L., Abedi, S., and Wu, W., Shear band in sand with spatially varying density, *J. Mech. Phys. Solids*, vol. **61**, no. 1, pp. 219–234, 2013.

Casagrande, A., Characteristics of cohesionless soils affecting the stability of slopes and earth fills, *Contrib. Soils Mech., 1925-1940*, vol. **23**, no. 1, pp. 13–32, 1936.

Cooreman, S., Lecompte, D., Sol, H., Vantomme, J., and Debruyne, D., Elasto-plastic material parameter identification by inverse methods: Calculation of the sensitivity matrix, *Int. J. Solids Struct.*, vol. **44**, no. 13, pp. 4329–4341, 2007.

Cosserat, E. and Cosserat, F., *Théorie des Corps Déformables*, Paris, 1909.

Dafalias, Y. F. and Manzari, M. T., Simple plasticity sand model accounting for fabric change effects, *J. Eng. Mech.*, vol. **130**, no. 6, pp. 622–634, 2004.

Desrues, J. and Andò, E., Strain localisation in granular media, *Comptes Rendus Physique*, vol. **16**, no. 1, pp. 26–36, 2015.

Desrues, J. and Viggiani, G., Strain localization in sand: An overview of the experimental results obtained in Grenoble using stereophotogrammetry, *Int. J. Numer. Anal. Methods Geomech.*, vol. **28**, no. 4, pp. 279–321, 2004.

Duhem, P., Le potentiel thermodynamique et la pression hydrostatique, In *Annales Scientifiques de l'École Normale Supérieure*, vol. **10**, pp. 183–230, 1893.

Ehlers, W., Ramm, E., Diebels, S., and d'Addetta, G. A., From particle ensembles to cosserat continua: Homogenization of contact forces towards stresses and couple stresses, *Int. J. Solids Struct.*, vol. **40**, no. 24, pp. 6681–6702, 2003.

Ehlers, W. and Scholz, B., An inverse algorithm for the identification and the sensitivity analysis of the parameters governing micropolar elasto-plastic granular material, *Arch. Appl. Mech.*, vol. **77**, no. 12, pp. 911–931, 2007.

Eringen, A. C., Theory of micropolar elasticity, In *Microcontinuum Field Theories*, pp. 101–248, Springer, Berlin, 1999.

Fish, J., Jiang, T., and Yuan, Z., A staggered nonlocal multiscale model for a heterogeneous medium, *Int. J. Numer. Methods Eng.*, vol. **91**, no. 2, pp. 142–157, 2012.

Flavigny, E., Desrues, J., and Palayer, B., Note technique: Le sable d'Hostun RF, *Revue. Fran. C Géotech.*, vol. **53**, pp. 67–70, 1990.

Gajo, A., Bigoni, D., and Wood, D. M., Multiple shear band development and related instabilities in granular materials, *J. Mech. Phys. Solids*, vol. **52**, no. 12, pp. 2683–2724, 2004.

Hall, S. A., Bornert, M., Desrues, J., Pannier, Y., Lenoir, N., Viggiani, G., and Bésuelle, P., Discrete and continuum analysis of localised deformation in sand using x-ray μct and volumetric digital image correlation, *Geotechnique*, vol. **60**, no. 5, pp. 315–322, 2010.

Herle, I. and Gudehus, G., Determination of parameters of a hypoplastic constitutive model from properties of grain assemblies, *Mech. Cohesive-Frictional Mater.*, vol. **4**, no. 5, pp. 461–486, 1999.

Hu, N. and Fish, J., Enhanced ant colony optimization for multiscale problems, *Comput. Mech.*, vol. **57**, no. 3, pp. 447–463, 2015.

Hughes, T. J. R., *The Finite Element Method: Linear Static and Dynamic Finite Element Analysis*, Courier Corporation, 2012.

Ikeda, K., Yamakawa, Y., and Tsutsumi, S., Simulation and interpretation of diffuse mode bifurcation of elastoplastic solids, *J. Mech. Phys. Solids*, vol. **51**, no. 9, pp. 1649–1673, 2003.

Issen, K. A. and Rudnicki, J. W., Conditions for compaction bands in porous rock, *J. Geophys. Res.: Solid Earth (1978–2012)*, vol. **105**, no. B9, pp. 21529–21536, 2000.

Kuhn, M. R., Sun, W., and Wang, Q., Stress-induced anisotropy in granular materials: Fabric, stiffness, and permeability, *Acta Geotech.*, vol. **10**, no. 4, pp. 399–419, 2015.

Lade, P. V. and Duncan, J. M., Elastoplastic stress-strain theory for cohesionless soil, *J. Geotech. Eng. Div.*, vol. **101**, no. 10, pp. 1037–1053, 1975.

Lasry, D. and Belytschko, T., Localization limiters in transient problems, *Int. J. Solids Struct.*, vol. **24**, no. 6, pp. 581–597, 1988.

Lenoir, N., Andrade, J. E., Sun, W. C., and Rudnicki, J. W., In situ permeability measurements inside compaction bands using x-ray CT and lattice Boltzmann calculations, *Adv. Comput. Tomography Geomater.: GeoX2010*, pp. 279–286, 2010.

Li, X. S. and Dafalias, Y. F., Anisotropic critical state theory: role of fabric, *J. Eng. Mech.*, vol. **138**, no. 3, pp. 263–275, 2011.

Lin, J. and Wu, W., A comparative study between DEM and micropolar hypoplasticity, *Powder Technol.*, vol. **293**, pp. 121–129, 2015.

Lin, J., Wu, W., and Borja, R. I., Micropolar hypoplasticity for persistent shear band in heterogeneous granular materials, *Comput. Methods Appl. Mech. Eng.*, vol. **289**, pp. 24–43, 2015.

Liu, Y., Sun, W., Yuan, Z., and Fish, J., A nonlocal multiscale discrete-continuum model for predicting mechanical behavior of granular materials, *Int. J. Numer. Methods Eng.*, vol. vol. **206**, no. 2, pp. 129–160, 2015.

Liu, Y., Sun, W., and Fish, J., Determining material parameters for critical state plasticity models based on multilevel extended digital database, *J. Appl. Mech.*, vol. **88**, no. 1, pp. 011003-1–16, 2016.

Mahnken, R. and Stein, E., A unified approach for parameter identification of inelastic material models in the frame of the finite element method, *Comput. Methods Appl. Mech. Eng.*, vol. **136**, no. 3, pp. 225–258, 1996.

Manzari, M. T. and Dafalias, Y. F., A critical state two-surface plasticity model for sands, *Geotechnique*, vol. **47**, no. 2, pp. 255–272, 1997.

Maugin, G. A. and Metrikine, A. V., Mechanics of generalized continua, *Adv. Mech. Math.*, vol. **21**, 2010.

Mindlin, R. D., Micro-structure in linear elasticity, *Arch. Rational Mech. Anal.*, vol. **16**, no. 1, pp. 51–78, 1964.

Molenkamp, F., Limits to the jaumann stress rate, *Int. J. Numer. Anal. Methods Geomech.*, vol. **10**, no. 2, pp. 151–176, 1986.

Na, S. and Sun, W., Wave propagation and strain localization in a fully saturated softening porous medium under the non-isothermal conditions, *Int. J. Numer. Anal. Methods Geomech.*, 2016.

Needleman, A., Material rate dependence and mesh sensitivity in localization problems, *Comput. Methods Appl. Mech. Eng.*, vol. **67**, no. 1, pp. 69–85, 1988.

Oda, M. and Iwashita, K., Study on couple stress and shear band development in granular media based on numerical simulation analyses, *Int. J. Eng. Sci.*, vol. **38**, no. 15, pp. 1713–1740, 2000.

Ortiz, M., Leroy, Y., and Needleman, A., A finite element method for localized failure analysis, *Comput. Methods Appl. Mech. Eng.*, vol. **61**, no. 2, pp. 189–214, 1987.

O'Sullivan, C., *Particulate Discrete Element Modelling*, Taylor & Francis, 2011.

Pestana, J. M. and Whittle, A. J., Formulation of a unified constitutive model for clays and sands, *Int. J. Numer. Anal. Methods Geomech.*, vol. **23**, no. 12, pp. 1215–1243, 1999.

Rechenmacher, A. L., Grain-scale processes governing shear band initiation and evolution in sands, *J. Mech. Phys. Solids*, vol. **54**, no. 1, pp. 22–45, 2006.

Roscoe, K. H., Schofield, A. N., and Wroth, C. P., On the yielding of soils, *Geotechnique*, vol. **8**, no. 1, pp. 22–53, 1958.

Rudnicki, J. W. and Rice, J. R., Conditions for the localization of deformation in pressure-sensitive dilatant materials, *J. Mech. Phys. Solids*, vol. **23**, no. 6, pp. 371–394, 1975.

Sadek, T., Lings, M., Dihoru, L., and Wood, D. M., Wave transmission in hostun sand: Multiaxial experiments, *Rivista Italiana Geotecnica*, vol. **41**, no. 2, pp. 69–84, 2007.

Satake, M., New formulation of graph-theoretical approach in the mechanics of granular materials, *Mech. Mater.*, vol. **16**, no. 1, pp. 65–72, 1993.

Schofield, A. and Wroth, P., Critical State Soil Mechanics, McGraw-Hill, p. 310, 1968.

Song, J.-H., Areias, P. M. A., and Belytschko, T., A method for dynamic crack and shear band propagation with phantom nodes, *Int. J. Numer. Methods Eng.*, vol. **67**, no. 6, pp. 868–893, 2006.

Subhash, G., Nemat-Nasser, S., Mehrabadi, M. M., and Shodj, H. M., Experimental investigation of fabric-stress relations in granular materials, *Mech. Mater.*, vol. **11**, no. 2, pp. 87–106, 1991.

Sun, W., A unified method to predict diffuse and localized instabilities in sands, *Geomech. Geoeng.*, vol. **8**, no. 2, pp. 65–75, 2013.

Sun, W. and Mota, A., A multiscale overlapped coupling formulation for large-deformation strain localization, *Comput. Mech.*, vol. **54**, no. 3, pp. 803–820, 2014.

Sun, W., Andrade, J. E., Rudnicki, J. W. and Eichhubl, P., Connecting microstructural attributes and permeability from 3D tomographic images of in situ shear-enhanced compaction bands using multiscale computations, *Geophys. Res. Lett.*, vol. **38**, no. 10, 2011.

Sun, W., Kuhn, M. R., and Rudnicki, J. W., A multiscale DEM-LBM analysis on permeability evolutions inside a dilatant shear band, *Acta Geotech.*, vol. **8**, no. 5, pp. 465–480, 2013.

Tejchman, J. and Niemunis, A., Fe-studies on shear localization in an anistropic micro-polar hypoplastic granular material, *Granular Matter*, vol. **8**, no. 3-4, pp. 205–220, 2006.

Walker, D. M., Tordesillas, A., and Kuhn, M. R., Spatial connectivity of force chains in a simple shear 3D simulation exhibiting shear bands, *J. Eng. Mech.*, p. C4016009, 2016.

Wang, K. and Sun, W., Anisotropy of a tensorial bishops coefficient for wetted granular materials, *J. Eng. Mech.*, p. B4015004, 2015.

Wang, K. and Sun, W., A semi-implicit micropolar discrete-to-continuum method for granular materials, In *VII European Congress on Computational Methods in Applied Science and Engineering*, 2016a.

Wang, K. and Sun, W., A semi-implicit discrete-continuum coupling method for porous media based on the effective stress principle at finite strain, *Comput. Methods Appl. Mech. Eng.*, vol. **304**, pp. 546–583, 2016b.

Wu, W., Bauer, E., and Kolymbas, D., Hypoplastic constitutive model with critical state for granular materials, *Mech. Mater.*, vol. **23**, no. 1, pp. 45–69, 1996.

Yang, Q., Mota, A., and Ortiz, M., A class of variational strain-localization finite elements, *Int. J. Numer. Methods Eng.*, vol. **62**, no. 8, pp. 1013–1037, 2005.